

Boosting Ferroptosis Therapy with Iridium Single-Atom Nanocatalyst in Ultralow Metal Content

Junjie Cheng,* Li Li, Duo Jin, Yi Dai, Yang Zhu, Jianhua Zou, Manman Liu, Wenxin Yu, Jiaji Yu, Yongfu Sun,* Xiaoyuan Chen,* and Yangzhong Liu*

Nanocatalysts are promising tumor therapeutics due to their ability to induce reactive oxygen species in the tumor microenvironment. Although increasing metal loading can improve catalytic activity, the quandary of high metal content versus potential systemic biotoxicity remains challenging. Here, a fully exposed active site strategy by site-specific anchoring of single iridium (Ir) atoms on the outer surface of a nitrogen-doped carbon composite (Ir single-atom catalyst (SAC)) is reported to achieve remarkable catalytic performance at ultralow metal content ($\approx 0.11\%$). The Ir SAC exhibits prominent dual enzymatic activities to mimic peroxidase and glutathione peroxidase, which catalyzes the conversion of endogenous H_2O_2 into $\cdot OH$ in the acidic TME and depletes glutathione (GSH) simultaneously. With an advanced support of GSH-trapping platinum(IV) and encapsulation with a red-blood-cell membrane, this nanocatalytic agent (Pt@IrSAC/RBC) causes intense lipid peroxidation that boosts tumor cell ferroptosis. The Pt@IrSAC/RBC demonstrates superior therapeutic efficacy in a mouse triple-negative mammary carcinoma model, resulting in complete tumor ablation in a single treatment session with negligible side effects. These outcomes may provide valuable insights into the design of nanocatalysts with high performance and biosafety for biomedical applications.

1. Introduction

Nanocatalytic therapy has emerged as an active frontier in tumor treatment due to its notable reactive oxygen species (ROS) generation efficiency and unique tumor-specific properties.^[1] A key concept in nanocatalyst design for biomedical applications is seeking nanocomponents with high activity, selectivity, and biosafety.^[2] It has been previously evidenced that the intrinsic character of the central metal, coordination environment, metal–support interaction, and metal loading cooperatively determine the performance of nanocatalysts.^[3] While increasing the number of active metal sites appears to be the most straightforward way to meet these goals,^[4] several major difficulties still exist. First, reactions take place only on the surface of nanocatalysts, therefore the active sites that act account for only a small fraction of the total metal contents.^[5] Simply increasing metal loading would easily

J. Cheng, D. Jin, M. Liu, W. Yu, J. Yu, Y. Liu
 Department of Chemistry
 Center for Bioanalytical Chemistry
 University of Science and Technology of China
 Hefei 230026, P. R. China
 E-mail: jjcheng2017@ustc.edu.cn; liuyz@ustc.edu.cn

L. Li, Y. Sun
 Hefei National Research Center for Physical Sciences at Microscale
 University of Science and Technology of China
 Hefei 230026, P. R. China
 E-mail: yfsun@ustc.edu.cn

Y. Dai
 College of Pharmaceutical Sciences
 Anhui Xinhua University
 Hefei 230001, P. R. China

Y. Zhu, J. Zou, X. Chen
 Departments of Diagnostic Radiology
 Surgery Chemical and Biomolecular Engineering and Biomedical Engineering
 Yong Loo Lin School of Medicine and College of Design and Engineering
 National University of Singapore
 Singapore 119074, Singapore
 E-mail: chen.shawn@nus.edu.sg

Y. Zhu, J. Zou, X. Chen
 Clinical Imaging Research Centre
 Centre for Translational Medicine
 Yong Loo Lin School of Medicine
 National University of Singapore
 Singapore 117599, Singapore

Y. Zhu, J. Zou, X. Chen
 Nanomedicine Translational Research Program
 NUS Center for Nanomedicine
 Yong Loo Lin School of Medicine
 National University of Singapore
 Singapore 117597, Singapore

Y. Zhu, J. Zou, X. Chen
 Institute of Molecular and Cell Biology
 Agency for Science
 Technology and Research (A*STAR)
 61 Biopolis Drive, Proteos, Singapore 138673, Singapore

 The ORCID identification number(s) for the author(s) of this article can be found under <https://doi.org/10.1002/adma.202210037>.

DOI: 10.1002/adma.202210037

lead to the agglomeration of active sites into clusters, thereby degrading catalytic performance.^[6] In addition, active metals are a double-edged sword and are thought to be the origin of potential biotoxicity in nanocatalysts. It may cause complex biophysicochemical interactions at the nanobio interfaces when exposed to physiological environments.^[7] Although some improved control strategies have been proposed to address biosafety issues recently,^[7a] such as improving the targeting of tumors and controlling metal ion release, increasing metal loading is still considered to raise the risk of systemic toxicity and adverse effects.^[1a] Taking all these factors into account, elevating metal availability within a limited metal content can be a feasible and straightforward way to alleviate these dilemmas.

Single-atom catalysts (SACs) are the catalysts that contain isolated individual atoms on solid supports accompanied by abundantly exposed active sites, which show a drastically boosted activity compared with their nanosized counterparts.^[8] Theoretically, the active sites are fully exposed, and the atom utilization efficiency of SACs can be up to 100%,^[3a,5] which is regarded as the limit of the precise design of nanomaterials at the atomic level.^[9] However, as mentioned above, the catalytic activity is mostly dominated by the surface atoms with minimal contributions from the inner core.^[5] Therefore, site-specific anchoring of metal atoms on the outer surface of supports could be a promising strategy to further improve catalytic performance, minimize metal use, and mitigate unwanted toxic side effects in biomedical applications.^[10] In addition to the manner of metal loading, the intrinsic activity of metal is more important to determine the catalytic performance of SACs. Iridium (Ir) is a precious metal belonging to platinum group elements, which is chemically stable and extremely resistant to corrosion. Owing to its multivalence and adsorption capacities to organic compounds, Ir shows excellent catalytic properties.^[11] Recently, Ir(III) complexes have attracted great attention in biomedical research due to their potential chemotherapeutic properties;^[12] however, the biomedical implications of Ir-based nanocatalysts has rarely been reported and need to be explored in depth.^[13] We proposed that the coordination and charge transfer potentials would be beneficial for Ir atoms in catalytic therapy, as those explored in nanozymes.^[14]

Here, we prepared iridium single atoms on a nitrogen-doped carbon composite (Ir_1/CN SAC) with an ultralow metal content and fully exposed active sites. The Ir_1/CN SACs exhibited notable peroxidase (POD)-like activity as well as high glutathione peroxidase (GSHOx)-like activity. The POD activity allows the catalysis of the conversion of endogenous H_2O_2 into $\cdot\text{OH}$ in the acidic tumor microenvironment (TME), while GSHOx activity causes the depletion of GSH, a cellular reductant that can eliminate ROS. Therefore, the synergistic effect of these two enzymatic activities results in significant ROS accumulation in tumor cells, which causes lipid peroxidation and subsequently leads to tumor cell ferroptosis. To further improve therapeutic efficacy, a novel GSH trapping platinum(IV) compound with anthraquinone ligands, denoted as Pt(IV) hereafter, was synthesized and loaded on Ir_1/CN SACs (Pt@IrSACs). The ligand anthraquinone, as a Michael acceptor, can react with cellular thiol group containing molecules, such as GSH to their α , β -unsaturated moiety system, perturb cellular redox homeostasis, and trigger the cell death.^[15]

The Pt@IrSACs was further encapsulated with the membrane of red blood cells (RBCs) (Pt@IrSACs/RBC) to improve biocompatibility and biodistribution of nanocatalysts in vivo. It is worth noting that, as a nitrogen-doped carbon composite, Ir_1/CN SACs showed remarkable photothermal performance upon irradiation in the near-infrared region (NIR) II window, which synergistically boosted the antitumor efficacies of catalytic therapy by photothermal effects (**Scheme 1**).

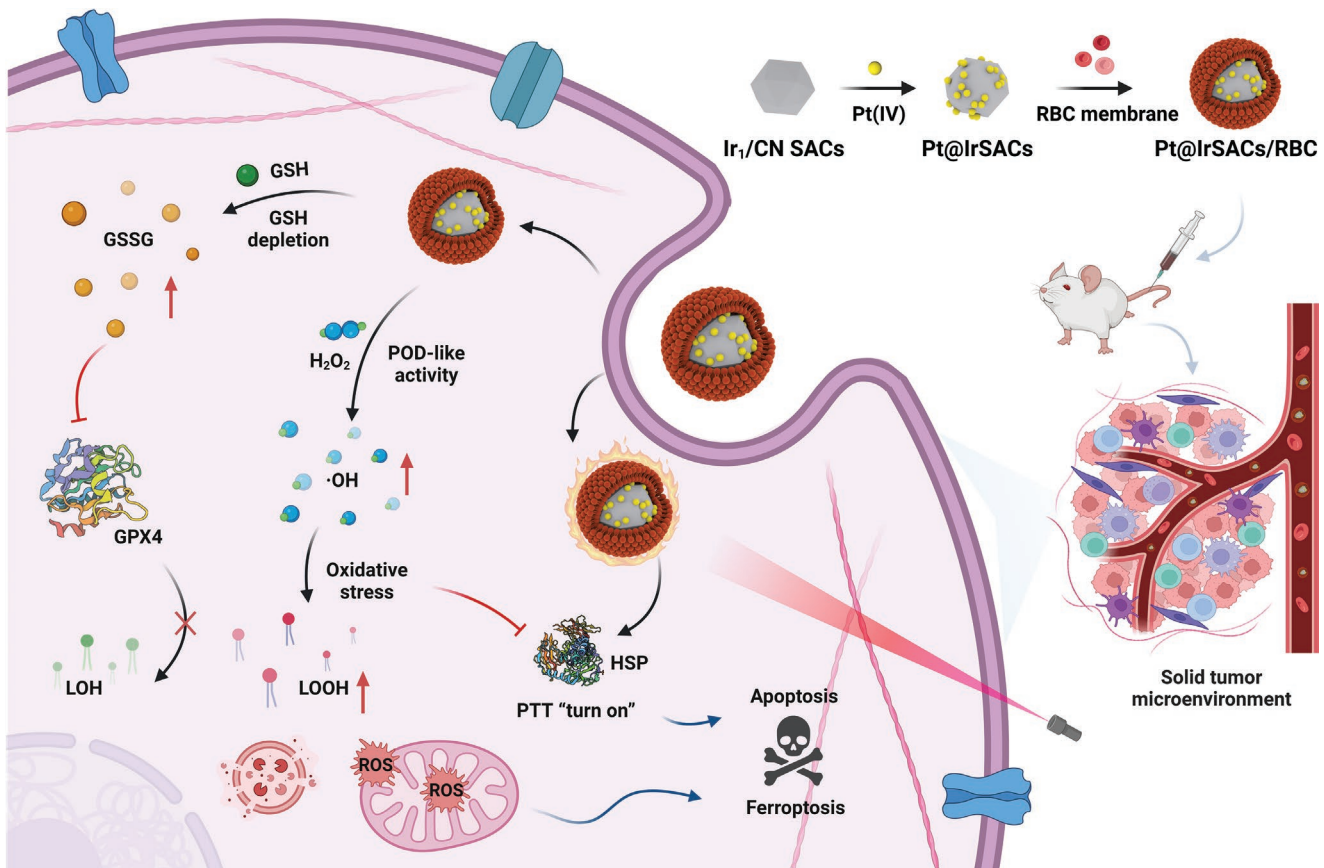
2. Results and Discussion

2.1. Preparation and Characterization of the Nanocatalyst

To realize the target of high reactivity with catalyst, we sought to fabricate an SAC with fully exposed active sites. The preparation of Ir_1/CN SAC is schematically illustrated in **Figure 1a**, including the three steps of in situ assembly of metal-organic units, surface ion exchange for loading Ir atoms, and pyrolysis to obtain the final porous Ir_1/CN SAC. Zeolite imidazolate framework-8 (ZIF-8) was first prepared and then supported with iridium species on the surface of ZIF-8 via an ion exchange process (Figure S1, Supporting Information). The transmission electron microscopy (TEM) images indicated that ZIF-8 and Ir-ZIF-8 nanoparticles were fabricated in rhombododecahedron morphology. The X-ray-diffraction pattern of Ir-ZIF-8 was well matched with that of pristine ZIF-8, indicating that the surface-loading of iridium species did not alter the crystallization of ZIF-8.^[16]

The Ir-ZIF-8 sample was then pyrolyzed to carbonize the organic linkers, and the iridium single atoms on the nitrogen-doped carbon composite (Ir_1/CN SAC) were obtained. During this process, the crystalline porous ZIF-8 host acted as a molecular fence and prevented the aggregation of iridium atoms. Moreover, the formed nitrogen-doped carbon can provide abundant coordination sites for iridium species to retrain a single-atom dispersion. The porous morphology of Ir_1/CN SAC with a slightly concave shape was observed after pyrolysis (Figure 1b and Figure S2, Supporting Information). The corresponding energy-dispersive spectrometry mapping demonstrated that Ir, N, and C atoms were homogeneously distributed in the Ir_1/CN SAC (Figure 1c,d). Inductively coupled plasma mass spectrometry measurement indicated that the Ir content was only $\approx 0.11\%$ w/w in Ir_1/CN SAC. The X-ray diffraction pattern of Ir_1/CN SAC showed two characteristic peaks of carbon at 25° and 44° (Figure S3, Supporting Information), which could be assigned to the conversion of organic carbon of ZIF-8 to crystalline CN. The graphitic structure of CN was further confirmed by Raman spectroscopy.^[17] To this end, X-ray photoelectron spectroscopy (XPS) revealed the dominant nitrogen species of pyrrolic and pyridinic nitrogen on CN host after pyrolysis (Figure S4, Supporting Information). Furthermore, Brunauer–Emmett–Teller measurement showed that the Ir_1/CN SAC processes a large surface area ($507 \text{ m}^2 \text{ g}^{-1}$; Figure S5, Supporting Information), which allows anchoring a large number of active sites on the surface of the CN support for efficient mass transport in catalytic reactions.

The states of iridium species over Ir_1/CN SAC were verified by atomic-resolution high-angle annular dark-field scanning transmission electron microscopy (HAADF-STEM) measurements. The single-atom dispersion of Ir atoms was clearly



Scheme 1. Schematic illustration of Pt@IrSAC/RBC application in tumor ferroptosis therapy. The scheme was created with Biorender.com.

observed (Figure 1e,f, bright dots labeled with white circles). The color contrasts confirmed an atomic dispersion of Ir species on the CN framework of Ir₁/CN SAC (Figure S6, Supporting Information). Moreover, Fourier-transformed extended X-ray absorption fine structure (EXAFS) analysis excluded Ir–Ir interactions, which further confirmed the single-atom dispersion of iridium species in Ir₁/CN SAC (Figure 1g). The X-ray absorption near-edge structure (XANES) spectra exhibited the average oxidation state of Ir⁴⁺ species with partial oxidation, which can be described by the intensity of the iridium L₃-edge (Figure 1h).^[18] The calculated oxidation state of iridium in Ir₁/CN which is 4.0 from the XANES spectra was further confirmed by XPS measurements (Figure S7, Supporting Information). Taken together, these results confirmed the successful synthesis of a single-atom dispersed Ir₁/CN SAC.

2.2. Construction of the Pt@IrSAC/RBC Nanoplatform

A cisplatin prodrug (Pt(IV)) containing anthraquinone ligands was synthesized via an active ester method (Figure S8, Supporting Information). The ¹H NMR spectrum of the Pt(IV) complex clearly showed the signals of anthraquinone groups (δ 8.33–8.06 (m, 6H), 7.92 (dt, J = 5.6, 2.2 Hz, 4H), 7.59 (t, J = 2.4 Hz, 2H), 7.46 (d, J = 7.3 Hz, 2H), 6.65 (s, 6H), 4.89 (s, 4H)), which indicated the successful ligation of anthraquinone

to Pt(IV) (Figures S9 and S10, Supporting Information). The presence of anthraquinone ligand sharply increases the lipophilicity of Pt(IV), which enabled the interaction of Pt(IV) with the hydrophobic surface of Ir₁/CN SAC through hydrophobic–hydrophobic interactions to generate the drug-loaded nanocatalyst Pt@IrSAC. To improve the stability and biocompatibility of Pt@IrSAC under physiological conditions, RBC membrane was employed to encapsulate nanoparticles to obtain the RBC membrane cloaked Pt@IrSACs (Pt@IrSACs/RBC). Since the basic scaffold of RBC membranes is amphipathic phospholipid bilayers embedded with proteins and other biomolecules, RBC membrane readily binds to hydrophobic nanomaterials via the hydrophobic layer and exposes its hydrophilic heads outside to enhance the dispersion and stability of nanoparticles in aqueous solution. The coating of RBC membrane on Pt@IrSACs can be observed intuitively under a TEM by the thick capping layers around the rhombododecahedron-shaped Ir₁/CN SAC particles (Figure 1i); meanwhile, the rough and porous surface of Ir₁/CN SACs morphology became smooth after RBC membrane encapsulation. Sodium dodecyl sulfate-polyacrylamide gel electrophoresis (SDS-PAGE) analysis showed that Pt@IrSACs/RBC contain the same protein strips as RBC membrane vesicles, indicating the successful coating of RBC membrane on the nanocatalysts (Figure S11, Supporting Information). The Pt content in Pt@IrSACs/RBC was measured using inductively coupled plasma-atomic emission spectrometry to be \approx 39.8 $\mu\text{g mg}^{-1}$.

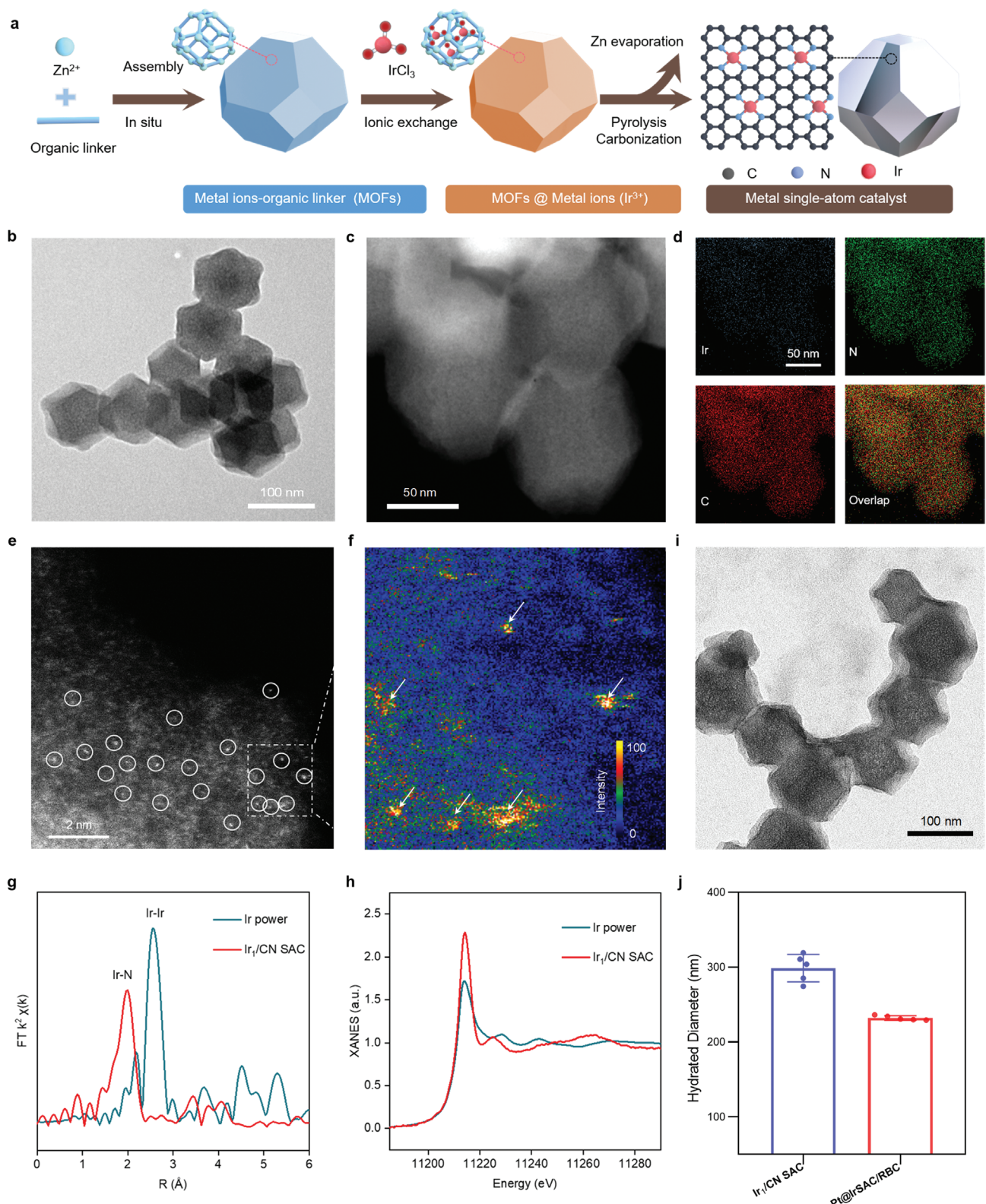


Figure 1. Synthesis and structural characterization of the Ir₁/CN SAC. a) A scheme for the fabrication of Ir₁/CN SAC via an ionic exchange strategy. b) TEM images of Ir₁/CN SAC. c) HAADF-STEM image. d) Corresponding energy-dispersive X-ray elemental mapping, which suggests the homogenous distribution of iridium (Ir), nitrogen (N), and carbon (C) in Ir₁/CN SAC. e,f) Atomic-resolution HAADF-STEM image and intensity maps with color profile, and the color contrasts confirm an atomic dispersion of Ir species on the CN framework. g) Fourier-transformed EXAFS signal of the experimental Ir₁/CN SAC along with reference samples. h) XANES of the Ir₁/CN SAC and reference samples. i) TEM of Pt@IrSAC/RBC. j) DLS analysis of hydrodynamic diameters of Ir₁/CN SACs and Pt@IrSACs/RBC.

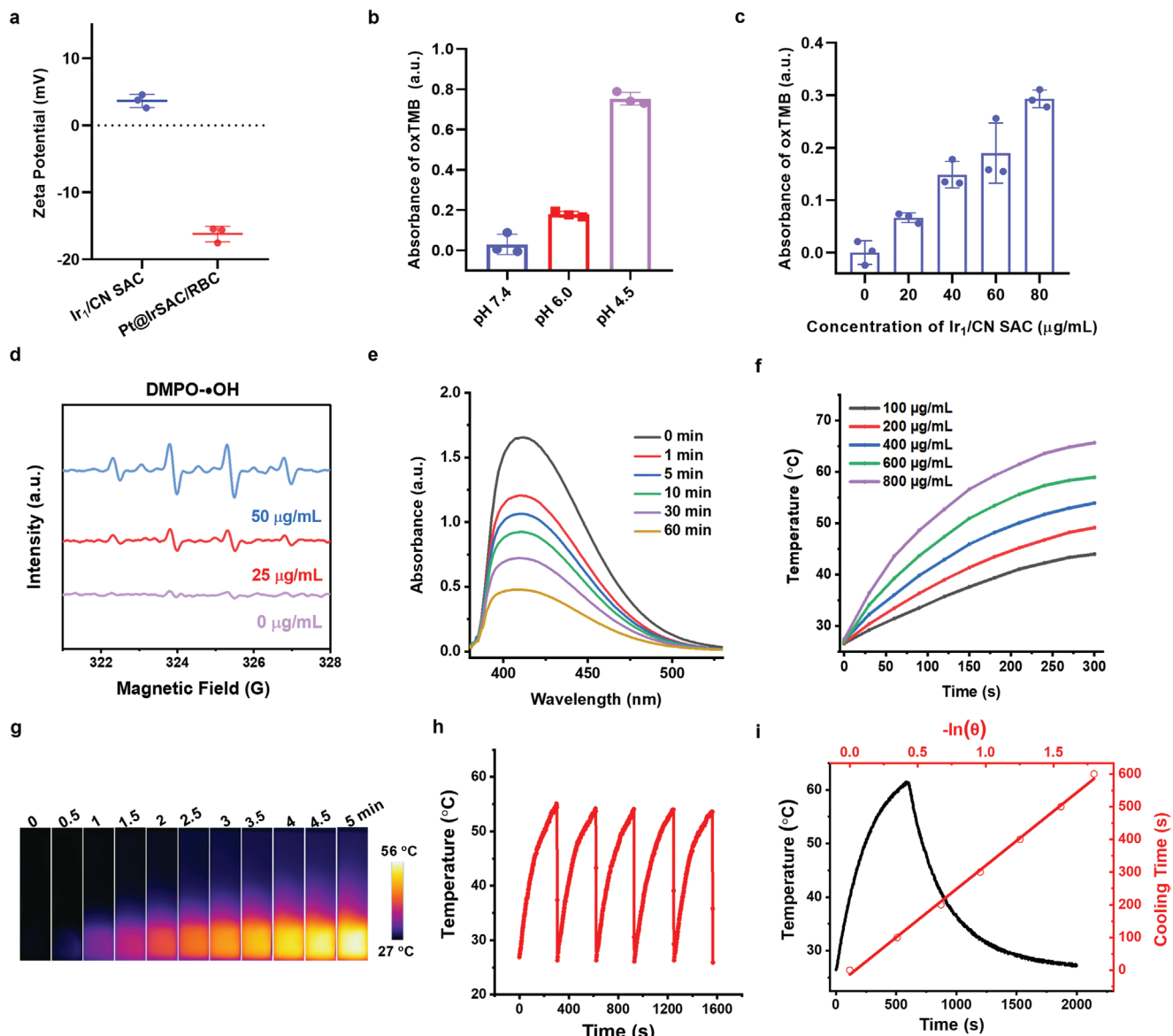


Figure 2. Characterization of Pt@IrSAC/RBC. a) Zeta potentials of Ir₁/CN SACs and Pt@IrSACs/RBC by DLS analysis. b) POD-like activity of Ir₁/CN SACs measured by TMB chromogenic reaction at pH 7.4, 6.0, and 4.5. c) POD-like activity of Ir₁/CN SACs by TMB chromogenic reaction. The concentration of Ir₁/CN SACs ranged from 0 to 80 µg mL⁻¹. d) ESR spectra detect •OH by using 1,3-diphenylisobenzofuran as a trapping agent. e) GSHOx catalytic property of Ir₁/CN SACs by DTNB reduction assay. The concentration of Ir₁/CN SACs was 400 µg mL⁻¹. f) The photothermal effect of RPt@Ir SACs under 1064 nm laser irradiation. The concentration of RPt@Ir SACs ranged from 100 to 800 µg mL⁻¹. g) IR thermal imaging of RPt@Ir SACs at different times. h) Temperature change profiles of RPt@Ir SACs with repeated irradiation cycles with a 1064 nm laser. i) Calculation of the photothermal conversion efficiency of RPt@Ir SACs. $\eta = 38.1\%$.

Dynamic light scattering (DLS) analysis showed that the hydrodynamic diameter of Ir₁/CN SACs was ≈298 nm (Figure 1j). The encapsulation of RBC membrane clearly decreased the hydrodynamic diameter of Pt@IrSACs/RBC by 66 nm. The reduced hydrodynamic diameter by RBC encapsulation is probably due to the fact that the RBC encapsulation can alter the thickness of hydration shell of Ir₁/CN SACs in the DLS measurement. Ir₁/CN SACs have a relatively larger hydration shell due to the presence of hydrophobic groups on their surface. By comparison, the RBC encapsulation generates a hydrophilic surface surrounding the nanocomposites; thus,

exhibiting a smaller hydrodynamic diameter in aqueous solution. As DLS measures the hydrodynamic size of the nanomaterial and its surrounding adsorbed layer of covering and solvent, the particle size is still bigger than the TEM result.^[19] Moreover, the hydrodynamic diameter of Pt@IrSACs/RBC remained unchanged for over 48 h in cell culture media (Figure S12, Supporting Information), indicating the high colloidal stability of the particles. In addition, the coating of negatively charged RBC membrane altered the zeta potential of Ir₁/CN SACs from +3.65 to -16.21 mV (Figure 2a), which would reduce the nonspecific interaction of the nanoparticles during the in vivo circulation.

2.3. The Catalytic Activity of the Nanocatalyst

Ir_1/CN SAC simultaneously mimic the catalytic activity of POD and GSHOx, which can decompose the endogenous H_2O_2 to $\cdot\text{OH}$ and deplete GSH to amplify the oxidative stress in cells. The POD-like activity of Ir_1/CN SAC was evaluated by a TMB assay using the chromogenic probe 3,3',5,5'-tetramethylbenzidine (TMB), as colorless TMB can be oxidized by $\cdot\text{OH}$ to form a blue ox-TMB.^[20] The results indicated that Ir_1/CN SAC exhibits negligible POD-like activity under neutral conditions; however, the activity increased significantly under weakly acidic conditions (Figure 2b). This result indicates the good selectivity of Pt@IrSACs/RBC in the acidic TME. Subsequently, the catalytic performance of Ir_1/CN SAC was further evaluated under the mild acidic condition (pH 6.0) to simulate the TME. As expected, the absorbance of ox-TMB was steadily enhanced with the increasing Ir_1/CN SAC from 0 to 80 $\mu\text{g mL}^{-1}$, validating the nanocatalyst-dependent ROS generation (Figure 2c). Similarly, changing the concentration of TMB and H_2O_2 showed a substrate-dependent catalytic reaction (Figures S13 and S14, Supporting Information). Since H_2O_2 is the major source of $\cdot\text{OH}$ generation, the decrease in H_2O_2 was quantified using the $\text{Ti}(\text{SO}_4)_2$ assay. The time-dependent decrease of absorbance indicates the consumption of H_2O_2 during the catalytic reaction (Figure S15, Supporting Information). To verify the ROS species in the reaction, electron spin resonance (ESR) spectra were recorded by using a specific $\cdot\text{OH}$ trap agent 5,5-dimethyl-1-pyrroline N-oxide. The characteristic quadruplet peaks with 1:2:2:1 intensity confirmed the production of $\cdot\text{OH}$ in the Ir_1/CN SAC catalyzed reactions (Figure 2d).

Tumor cells typically contain abundant endogenous GSH that can scavenge ROS produced by catalytic reactions and weaken the therapeutic efficacy. The GSHOx-mimicking activity enables Ir_1/CN SAC to deplete GSH, enhancing the effect of catalytic therapy. GSH depletion by Ir_1/CN SAC was studied by 5,5'-dithiobis (2-nitrobenzoic acid) (DTNB) reduction assay. DTNB is a thiol probe that can react with GSH and form yellow-colored 5-thio-2-nitrobenzoic acid (TNB). As depicted in Figure 2e, the absorbance of TNB (412 nm) gradually decreased in the DTNB reduction assay over time, reflecting the effective GSHOx-like activity of Ir_1/CN SAC. Notably, the anthraquinone ligand of Pt(IV) contains α,β -unsaturated aldehydes and ketones that can form covalent bonds with thiol groups via a Michael addition reaction;^[21] hence, DTNB assay showed that Pt(IV) complex is able to deactivate GSH based on reduced absorption of TNB (Figure S16, Supporting Information). Thus, the Pt@IrSAC/RBC formula, with the combination of GSHOx-mimicking activity of Ir_1/CN SAC and GSH-deactivation of Pt(IV), demonstrated synergistic effect on GSH depletion. This effect can be clearly detected by the DTNB assay, which caused more significant GSH depletion than either Ir_1/CN SAC or Pt(IV). Therefore, Pt@IrSACs/RBC possess great potential to elevate oxidative stress in the acidic TME by inducing $\cdot\text{OH}$ accumulation together with inhibiting ROS scavenging by GSH depletion.

2.4. The Photothermal Performance of Pt@IrSAC/RBC

Apart from the dual catalytic activities, the amorphous carbon and nitrogen structure endows the material with considerable

photothermal performance.^[22] The Ir_1/CN SAC showed a broad absorption feature from 700 to 1300 nm, suggesting that the nanocatalyst could be applied as a photothermal agent for photothermal therapy (PTT) in the NIR region (Figure S17, Supporting Information). Since NIR II window (1000–1400 nm) confers an apparent therapeutic advantage over NIR I (750–1000 nm), such as the deeper tissue penetration depth and higher maximum permissible exposure,^[23] a 1064 nm (the commonly used NIR II wavelength) laser was selected to investigate the photothermal conversion property of Pt@IrSACs/RBC. The heating curves showed that the temperature raised faster with higher concentrations of Pt@IrSACs/RBC under laser irradiation (1064 nm at 1W cm^{-2} for 300 s); and Pt@IrSACs/RBC was sufficient to reach the effective therapeutic temperature (42 °C)^[24] for tumor hyperthermia treatment (Figure 2f). The positive correlation between temperature and irradiation power can be observed in Figure S18 in the Supporting Information. The Pt@IrSACs/RBC reached 55 °C within 300 s under laser irradiation at 1W cm^{-2} , which was adequate for tumor PTT. The good photothermal performance can also be intuitively reflected by IR thermal images, and the time-dependent heating indicates the effective conversion of optical energy into thermal energy by Pt@IrSACs/RBC (Figure 2g). In addition, negligible photothermal deterioration was observed during five ON/OFF laser cycles, showing the high photothermal stability of Pt@IrSACs/RBC (Figure 2h). In general, the photothermal conversion efficiency (η) of photothermal agents directly affects the therapeutic outcome.^[25] The photothermal conversion efficiency of Pt@IrSACs/RBC was calculated to be 38.1% following the Roper's method (Figure 2i),^[26] which is significantly higher than that of commercial photothermal reagents, such as indocyanine green (3.1%),^[27] suggesting the good photothermal conversion property of Pt@IrSACs/RBC that can be used as a photothermal agent for cancer therapy.

2.5. In Vitro Catalytic Performance of Pt@IrSACs/RBC

To investigate the nanobiointeraction of the nanocatalyst with 4T1 breast tumor cells, cellular uptake behavior was monitored first by tracking a Nile Red-labeled Ir_1/CN SAC coating with RBC membrane (RN@IrSAC/RBC) in cells. RN@IrSAC/RBC was readily endocytosed by 4T1 cells, which exhibited bright red fluorescence in the cytoplasm (Figure 3a). Notably, the DNA platination level of cells incubated with Pt@IrSACs/RBC was ≈ 2.3 times higher than that of free Pt(IV), indicating the favorable internalization of nanoagents by tumor cells (Figure S19, Supporting Information). After verifying the effective cellular internalization of RBC-membrane-coated Ir_1/CN SACs (IrSACs), the ROS accumulation catalysis and photothermal effect of Pt@IrSACs/RBC were investigated. A green fluorescence indicator, 2,7-dichlorofluorescein diacetate (DCFH-DA), was used to assess the intracellular ROS levels. As shown in Figure 3b, the Pt(IV) treatment increased relative fluorescence intensity of the cells from 3.45% to 13.51%, which can be attributed to the inactivation of free thiol by Pt(IV) that perturbed the intracellular redox homeostasis. IrSACs increased the fluorescence to 25.11%, indicating the efficient catalytic effects of nanocatalysts in tumor cells. As expected, Pt@IrSACs/RBC caused

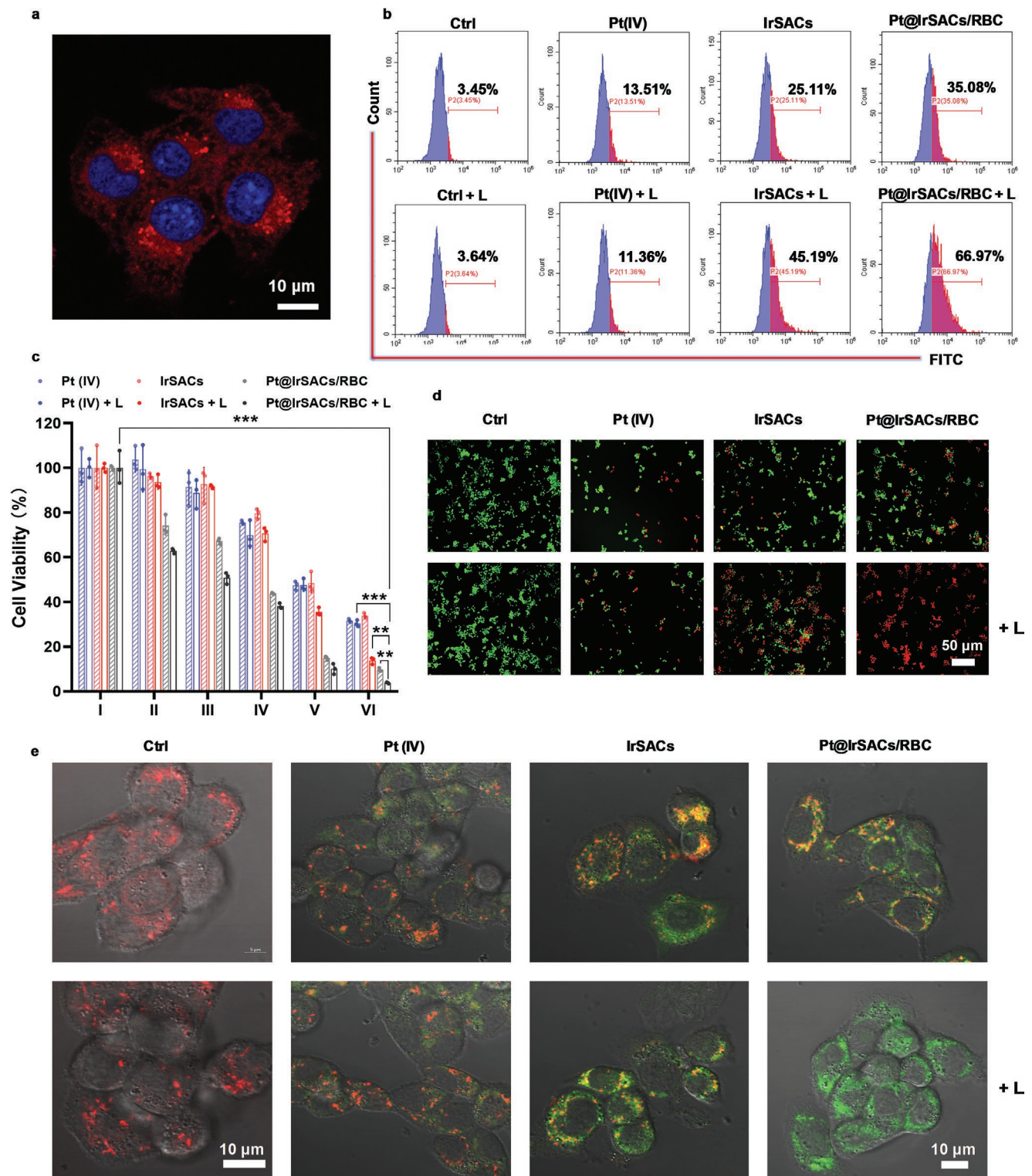


Figure 3. In vitro catalytic performance of Pt@IrSAC/RBC. a) Confocal microscopy images of 4T1 cells post-incubation with RN@IrSACs/RBC (red: RN@IrSAC/RBC, blue: nucleus). b) Analysis of ROS levels in 4T1 cells using DCFH-DA staining by flow cytometry. 4T1 cells were treated with Pt(IV), IrSACs, and Pt@IrSACs/RBC for 8 h with or without laser irradiation (1 W cm^{-2} , 5 min). c) Cell viability of 4T1 cells post-treatment with Pt(IV), IrSACs, and Pt@IrSACs/RBC for 48 h with (indicated with + L) or without laser irradiation (1 W cm^{-2} , 5 min). The concentrations of Pt@IrSAC/RBC were: I) 3.13, II) 6.25, III) 12.5, IV) 25, V) 50, and VI) 75 $\mu\text{g mL}^{-1}$. * $p < 0.05$, ** $p < 0.01$, *** $p < 0.001$. Statistical analyses were conducted using t-test. d) Live/dead co-stained 4T1 cells treated with Pt(IV), IrSACs, and Pt@IrSACs/RBC for 24 h with or without laser irradiation (1 W cm^{-2} , 5 min). e) Confocal laser scanning microscopy images were used to analyze mitochondrial depolarization with a JC-1 kit. 4T1 cells were treated with Pt(IV), IrSACs, and Pt@IrSACs/RBC for 8 h with or without laser irradiation (1 W cm^{-2} , 5 min).

most intensive ROS generation (35.08%) compared with Pt(IV) or IrSACs alone, suggesting that Pt(IV) is capable of facilitating the catalytic efficacy of IrSACs. By using simultaneous photothermal-catalytic therapy, improved ROS generation efficiency was achieved in both IrSACs and Pt@IrSACs/RBC treated cells (45.19% and 66.97%, respectively), illustrating the superiority of the combined therapy (Figure S20, Supporting Information). Similar results were also obtained by fluorescence microscopy analysis (Figure S21, Supporting Information).

The cytotoxicity of Pt@IrSAC/RBC was assessed by a methyl thiazolyl tetrazolium assay. As shown in Figure 3c, cell viability obviously decreased after treatment with Pt(IV) and IrSAC, especially at high concentrations; and Pt@IrSAC/RBC showed a more intense therapeutic effect than the single Pt(IV) or IrSACs, indicating the ability of Pt(IV) to further amplify the oxidative injury by IrSACs. This effect became more effective with laser irradiation. IrSAC plus laser treated cells exhibited \approx 14% survival at a dose of 75 μ g mL⁻¹, while the treatment with Pt@IrSAC/RBC plus laser showed the best therapeutic effect, obtaining \approx 96% tumor cell inhibition, which demonstrated the potent efficacy of Pt@IrSACs/RBC for combining catalytic therapy and PTT. Similar results can be obtained via live/dead cell stain analysis. After treatment with different therapeutic agents, cells were co-stained with propidium iodide (red fluorescence on dead cells) and fluorescein diacetate (green fluorescence on live cells). The fluorescence images showed that more red fluorescence appeared on cells treated with Pt@IrSACs/RBC; and nearly all the green fluorescence vanished with cells exhibiting predominant red fluorescence in Pt@IrSACs/RBC with NIR irradiation group (Figure 3d). Overall, the catalytic and photothermal combination strategy may maximize the antitumor effect of Pt@IrSACs/RBC.

To investigate whether the Pt@IrSAC/RBC-induced cell death is associated with ROS-mediated damage mechanisms, the mitochondrial depolarization and lysosome disruption analyses were performed.^[28] The mitochondrial membrane potential (MMP) was studied by using a mitochondrial fluorescence probe 5,5',6,6'-tetrachloro-1,1',3,3'-tetraethyl-imidacarbocyanine iodide (JC-1), which emits red fluorescence in intact mitochondria or emits green fluorescence in depolarized mitochondria.^[29] The damage to the mitochondrial membrane by Pt(IV) was confirmed by the appearance of green fluorescent signals, which can be explained by the oxidative damage caused by GSH inactivation as well as platinum complexes-induced apoptosis (Figure 3e).^[30] The partial MMP loss that detected in IrSACs treated group exhibited distinct green fluorescence in tumor cells; and unsurprisingly, Pt@IrSACs/RBC induced more green signals, which were then accompanied by an almost disappearing red fluorescent signal after exposure to laser irradiation, reflecting the complete loss of MMP. Furthermore, lysosome integrity was studied by assessing the cellular retention of acridine orange (AO). AO is a pH-sensitive dye that highly concentrates in acidic lysosomes resulting in red fluorescence, and shifts to green fluorescence after leaking into the neutral cytoplasm.^[31] The amount of red fluorescence decreased sequentially in Pt(IV), IrSACs, and Pt@IrSACs/RBC groups, revealing the increased degree of lysosomal membrane disruption (Figure 4a). Consistent with the mitochondrial depolarization results, the red fluorescence almost completely

disappeared after laser exposure following Pt@IrSACs/RBC treatment, suggesting the full disruption of lysosomal membrane. These experimental results demonstrated that the Pt@IrSACs/RBC could significantly raise intracellular oxidative stress levels to induce cell death by simultaneously catalyzing the •OH generation and GSH depletion, and this effect could be further enhanced by NIR exposure.

2.6. Pt@IrSACs/RBC-Induced Cell Ferroptosis

Ferroptosis is a nonapoptotic form of programmed cell death characterized by iron-dependent intracellular accumulation of lipid hydroperoxide abundance. Ferroptosis-based cancer therapy, which is able to bypass drug resistance mediated by the apoptotic pathway, shows great potential from traditional apoptotic therapeutics.^[32] As Pt@IrSACs/RBC-induced cell death is directly related to cellular ROS elevation, we further verified that whether this process is associated with ferroptosis by evaluating the three key events in ferroptosis, including lipid peroxidation, GSH depletion, and oxidation accumulation. First, the lipid peroxidation was evaluated by using a green fluorescent probe BODIPY-C11.^[32a] The results in Figure 4b showed that Pt@IrSACs/RBC caused a noticeable accumulation of lipid peroxides (LPO), which exhibited pronounced green fluorescence in 4T1 cells. Again, this effect was further promoted via the combinational treatment of nanocatalyst and NIR exposure, which elevated LPO levels, a key feature in ferroptosis. Thus, mitochondrial shrinkage, the characteristic consequence of ferroptosis, was observed in cells treated with Pt@IrSACs/RBC as expected (Figure 4c and Figure S22, Supporting Information). Subsequently, the intracellular GSH level was assessed via the DTNB assay. The Pt@IrSACs/RBC elicited a dramatic decrease in GSH levels down to 50% of the control group; and it further fell even to 10% with further irradiation (Figure 4d). Since GSH is an ROS scavenger ROS that maintains cellular redox balance,^[33] the gross consumption of GSH results in oxidation accumulation in cells. Thus, the abundance of malondialdehyde (MDA), another marker of oxidative stress and LPO was analyzed.^[34] As indicated in Figure 4e, Pt@IrSACs/RBC significantly increased MDA levels by 2.4-fold, and this level further rose to 2.8-fold by laser irradiation, indicating the exposure of tumor cells to high levels of oxidative stress.

Next, we sought to identify the signaling pathway that ROS modulate in cell ferroptosis. GPX4 is a GSH-dependent peroxidase that catalyzes the reduction of lipid peroxides,^[35] and interference with the function of GPX4 induces lipid ROS accumulation and results in ferroptosis.^[36] Considering the importance of GSH to the proper function of GPX4, we hypothesized that the continuous depletion of GSH through Pt@IrSACs/RBC would downregulate the GPX4 level in cells. Western blotting results showed that the GPX4 expression significantly decreased in cells treated with Pt@IrSACs/RBC (Figure 4f). The quantified results showed that, after laser irradiation, the GPX4 expression in the Pt@IrSACs/RBC treated cells was only about 28% of that of control group (Figure S23, Supporting Information). These analyses reveal that Pt@IrSACs/RBC-induced cell death intimately associated with the GPX4-dependent ferroptosis. Notably, a significant decrease in intracellular SOD1 and

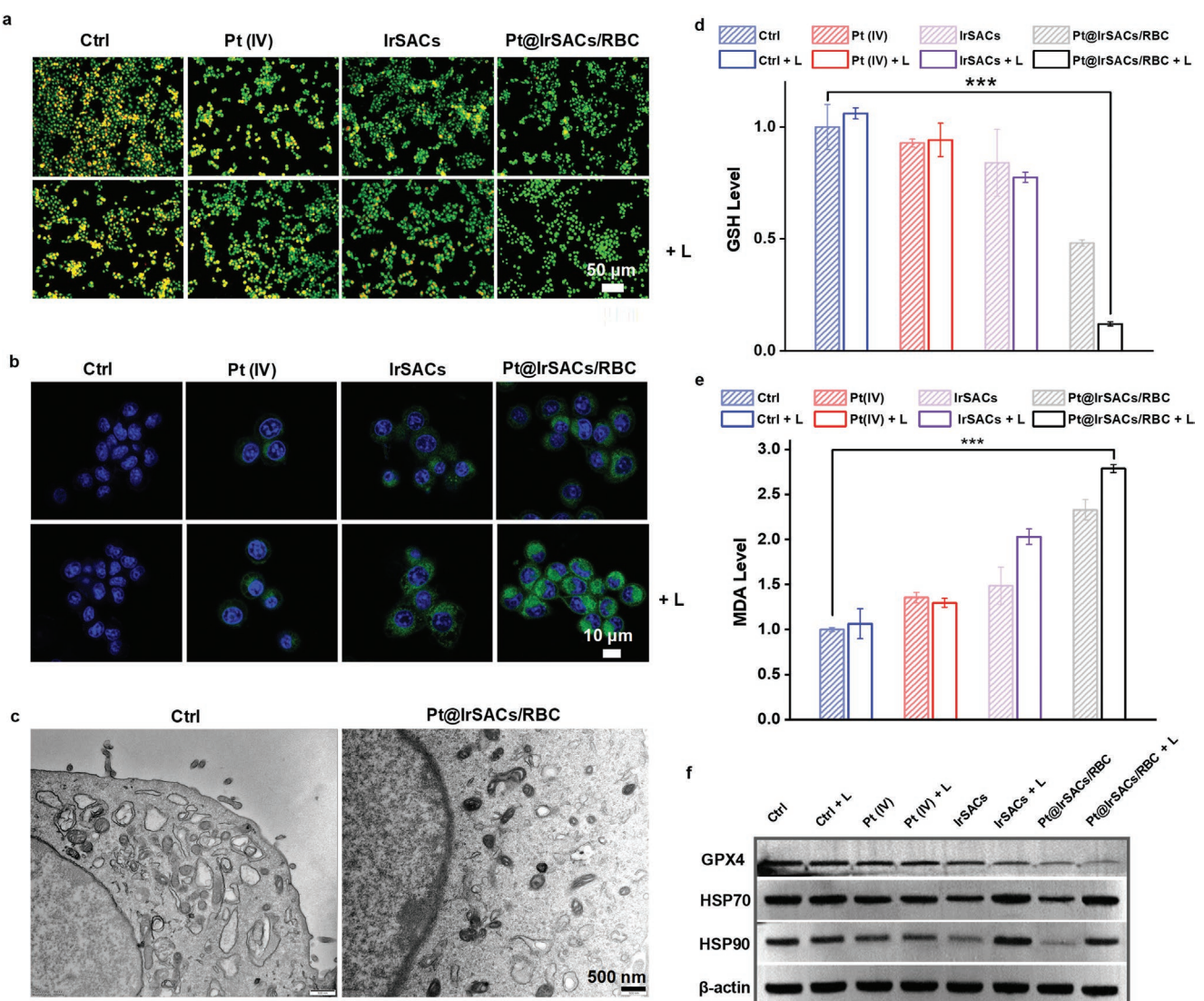


Figure 4. Potential antitumor mechanism of Pt@IrSACs/RBC. a) Fluorescence images of 4T1 cells stained with AO after incubation with Pt(IV), IrSACs, and Pt@IrSACs/RBC at an equivalent Pt concentration of 15×10^{-6} M with (indicated with +L) or without laser irradiation (1 W cm^{-2} , 5 min). b) Lipid peroxide measured by BODIPY-C11 staining in 4T1 cells after incubation with Pt(IV), IrSACs, and Pt@IrSACs/RBC at the equivalent Pt concentration of 15×10^{-6} M with (indicated with +L) or without laser irradiation (1 W cm^{-2} , 5 min). c) TEM imaging of cellular morphology after treatment with Pt@IrSACs/RBC for 24 h. d) GSH level of 4T1 cells after incubation with Pt(IV), IrSACs, and Pt@IrSACs/RBC at the equivalent Pt concentration of 15×10^{-6} M with (indicated with +L) or without laser irradiation (1 W cm^{-2} , 5 min). e) MDA level of 4T1 cells after incubation with Pt(IV), IrSACs, and Pt@IrSACs/RBC at the equivalent Pt concentration of 15×10^{-6} M with (indicated with +L) or without laser irradiation (1 W cm^{-2} , 5 min). f) Western blot analysis of GPX4, HSP 70, and HSP 90 expression in 4T1 cells post-treatment with Pt(IV), IrSACs, and Pt@IrSACs/RBC at the equivalent Pt concentration of 15×10^{-6} M with (indicated with +L) or without laser irradiation (1 W cm^{-2} , 5 min).

SOD2 levels was also detected in the Pt@IrSACs/RBC treated cells, suggesting that the Pt@IrSACs/RBCs-induced cellular oxidative stress was also related to its interference with endogenous ROS scavengers (Figure S24, Supporting Information). In addition, the expression of heat shock proteins (HSPs) 70 and 90 was also monitored since the upregulation of HSPs improves the survival of tumor cells under heat stress.^[37] The results showed that the laser irradiation has only a marginal effect on the expression of HSP70 and HSP90 in Pt@IrSACs/RBC treated cells, which would allow Pt@IrSAC/RBC to be an efficient nanoagent for tumor cells killing (Figure 4f and Figures S25 and S26, Supporting Information). This effect could

be associated with the ROS generation of Pt@IrSACs/RBC, as HSPs can be cleaved by the accumulation of ROS.^[37] Taken together, these results indicated a favorable combination of catalytic therapy and PTT by using Pt@IrSACs/RBC.

2.7. In Vivo Biodistribution and Photothermal Behavior of RBC-Membrane-Coated Ir1/CN SACs

The formation of protein corona is a challenge for nanomaterials in biomedical applications since hard coronas could significantly deactivate the function of nanocatalysts because of

steric blocking of the active sites.^[38] To overcome this predicament, RBC membrane was coated on Ir₁/CN SACs in order to prevent formation of protein corona, since RBC membrane capped nanoparticles hardly adsorbed proteins in plasma.^[39] To test this hypothesis, the potential interaction between Pt@IrSACs/RBC and living matter in a physiological environment was first explored in human, bovine, and mice plasma. After removal of the unbound and loosely bound proteins, the protein coronas were analyzed by SDS-PAGE (Figure S27, Supporting Information). The results showed that the number of proteins bound to Pt@IrSACs/RBC were significantly less than those to the naked Ir₁/CN SACs, suggesting that RBC membrane can markedly reduce the shielding effect of the blood macromolecules to the Ir₁/CN SACs and effectively avoid the unwanted inactivation of nanocatalysts.

Apart from preventing the formation of protein coronas, natural RBC membrane also exhibits advantages over non-natural protectors, including the gold standard stealth coating, poly(ethylene glycol) (PEG), especially considering the recent observation of anti-PEG immunological response.^[40] As an inherently suited carrier for intravascular administration, RBC membrane is expected to reduce the phagocytosis of nanomaterials by the reticuloendothelial system and prolong their circulation time *in vivo*.^[41] To verify the advantages of RBC membrane protection, the *in vivo* biodistribution of nanocatalysts was spatiotemporally tracked with fluorescence imaging on the NIR fluorescent dye IR780 loaded Ir₁/CN SACs with/without RBC membrane protection (denoted as 780@IrSAC/RBC and 780@IrSACs, respectively). As shown in Figure 5a, fluorescence signal in tumor was observed 4 h post-injection of 780@IrSACs/RBC, and gradually increased and reached the peak at 24 h in tumor region. In comparison, the signal of 780@IrSACs was not observed in tumor until 12 h post-injection, and then reduced greatly ≈48 h post-injection (Figure S28, Supporting Information). This result highlights the advantage of RBC membrane coating on Ir₁/CN SACs in tumor accumulation and retention. It is worth noting that, compared with the other major organs, 780@IrSACs/RBC signal remained significantly higher in tumor site even at 48 h post-injection (Figure S29, Supporting Information), which can be attributed to the enhanced permeability and retention property of nanoparticles and long-circulation effect from RBC membranes.^[42] This result can be also obtained through biodistribution study that measured by the concentration of Pt in major organs after injection of Pt@IrSACs/RBC (Figure S30, Supporting Information). This advantage of nanoagent is particularly evident compared with free IR780 (Figure S28, Supporting Information). This suggests that RBC-membrane-coated Ir₁/CN SACs exhibited superior blood retention and circulation lifetime compared to the naked nanomaterials and free drugs, which confirmed the immune-evasive functionality of RBC membrane that enhanced tumor enrichment and improved biodistribution *in vivo*.^[43] The result of time-dependent accumulation and biodistribution of Pt@IrSACs/RBC allowed effective PTT in an optimal time window. The photothermal imaging showed that the treatment of Pt@IrSAC/RBC resulted in a rapid temperature increase of 20 °C in tumor site with 10 min NIR laser irradiation (Figure 6b and Figures S31 and S32, Supporting Information). This result indicates that Pt@IrSAC/RBC is well suitable for *in vivo* PTT of tumors.

2.8. In Vivo Antitumor Efficacy of Pt@IrSACs/RBC

The therapeutic formulations were injected intravenously into 4T1-tumor-bearing mice to evaluate their antitumor efficacy. The mice were randomly divided into six groups, Phosphate-buffered saline (PBS, group I), Pt(IV) (group II), IrSACs (group III), IrSACs plus laser (group IV), Pt@IrSAC/RBC (group V), and Pt@IrSAC/RBC plus laser (group VI). The treated protocol is illustrated in Figure 5c, only one intravenous injection was included in the treatment regimen followed by a 1064 nm laser exposure for 10 min at 24 h post-injection. The body weight and tumor volume of mice were collected every other day during the 14 days treatment. The tumor volume curves showed that, compared with PBS group, the groups II, III, and V all have a significant influence on the suppression of tumor growth (Figure 5d). Moreover, the therapeutic efficacy of IrSACs and Pt@IrSAC/RBC can be further enhanced by applying laser irradiation to tumors. The tumors in groups IV and VI were eradicated on the 4th day after treatment, indicating the high efficiency of the combination treatment. All the mice in group VI remained tumor-free for the entire monitoring period. However, tumor recurrence was identified in group IV on the 8th day (Figure 5e and Figures S33 and S34, Supporting Information). These results could be due to that the tumors are more sensitive to the synergistic effects of nanocatalysts with chemotherapeutic agents. The addition of Pt(IV) greatly amplified the therapeutic potency and persistence of IrSACs. The survival curve showed that all mice in group VI survived in 60 days post-administration, indicating that the Pt@IrSAC/RBC plus laser is a promising therapeutic strategy for tumor treatment (Figure 5f).

The enhanced catalytic and photothermal efficacy was further evaluated through the terminal deoxynucleotidyl transferase-mediated deoxyuridine triphosphate nick end labeling (TUNEL) staining assay, hematoxylin and eosin (H&E) staining assay, caspase 3, and Ki67 levels. Consistent with the tumor suppression results, the tumor in Pt@IrSAC/RBC plus laser group showed the most positive cells with green fluorescence in TUNEL staining images, revealing the massive tumor cell apoptosis after treatment (Figure 5g). Similar results of tumor tissue damage were also obtained from H&E staining (Figure S35, Supporting Information) and caspase 3 level (Figure S36, Supporting Information). The Ki67 expression was also decreased significantly in group VI, suggesting that the proliferative capacity of tumor was inhibited (Figure S37, Supporting Information). To confirm the role of ferroptosis in Pt@IrSAC/RBC-induced cell death, the expression of GPX4 was analyzed. The protein expression of GPX4 was clearly decreased by the Pt@IrSAC/RBC combined with 1064 nm laser administration, which indicated the occurrence of ferroptosis (Figure 5h). Moreover, the immunohistochemistry of HSP70 on tumor tissues were also monitored to confirm the inhibitory effect of Pt@IrSAC/RBC in the tumor heat stress response. As presented in Figure 5i, the level of HSP70 did not show a significant increase in the Pt@IrSAC/RBC plus laser group, compared to the control, which can be attributed to the balance between the activation heat shock response in tumors and the inhibition of HSP expression by ROS accumulation.

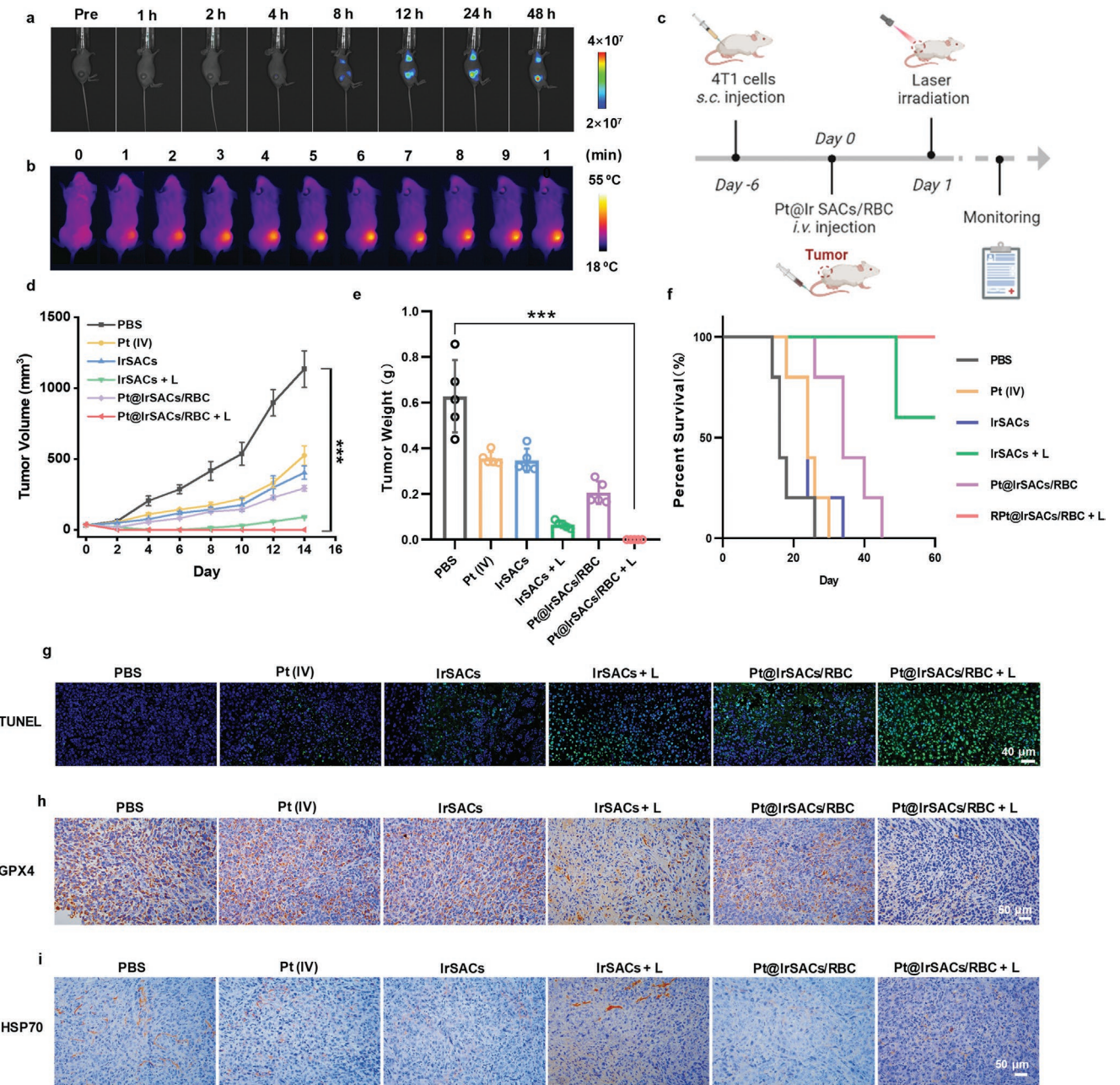


Figure 5. Efficient therapeutic efficacy against murine 4T1 tumors by Pt@IrSAC/RBC. **a)** Real-time biodistribution images of 780@IrSAC/RBC before and after injection. **b)** In vivo IR thermal imaging images of 4T1-tumor-bearing mice treated with 15 mg kg^{-1} Pt@IrSAC/RBC after 24 h injection upon 1064 nm laser irradiation. **c)** Illustration of treatment schedule. Nanoagents were administered intravenously at a dose of 15 mg kg^{-1} once only with or without 1064 nm irradiation post 24 h injection. The dosage of Pt(IV) was consistent with the Pt content of Pt@IrSAC/RBC. **d-f)** Mice were monitored for tumor growth (**d,e)** and survival (**f**). **g-i)** Histological microscopic images. The dissected tumors were stained with TUNEL (blue fluorescence: Hoechst; green fluorescence: TUNEL) (**g**), GPX4 (**h**), and HSP 70 (**i**). Figure 5c was created with Biorender.com.

2.9. The Biosafety of Pt@IrSACs/RBC

Since good biosafety is a major prerequisite for biomedical nanoagents,^[44] the biocompatibility and safety of Pt@IrSACs/RBC were assessed in detail. As shown in Figure 6a, each treatment has little effect on the body weight of mice, implying that all the administration was well tolerated. Next, the hemolysis assay of Pt@IrSAC/RBC at various concentra-

tions was performed (Figure 6b). No apparent hemolysis was found even at high concentrations ($800 \mu\text{g mL}^{-1}$), ensuring the safety of Pt@IrSAC/RBC for vein injection. Following this, the liver and kidney function of mice were evaluated by blood biochemistry test. During the 14 days administration, the levels of typical markers including the blood urea nitrogen (BUN), alanine aminotransferase (ALT), aspartate aminotransferase (AST), alkaline phosphatase (AKP), and creatinine (CRE) were

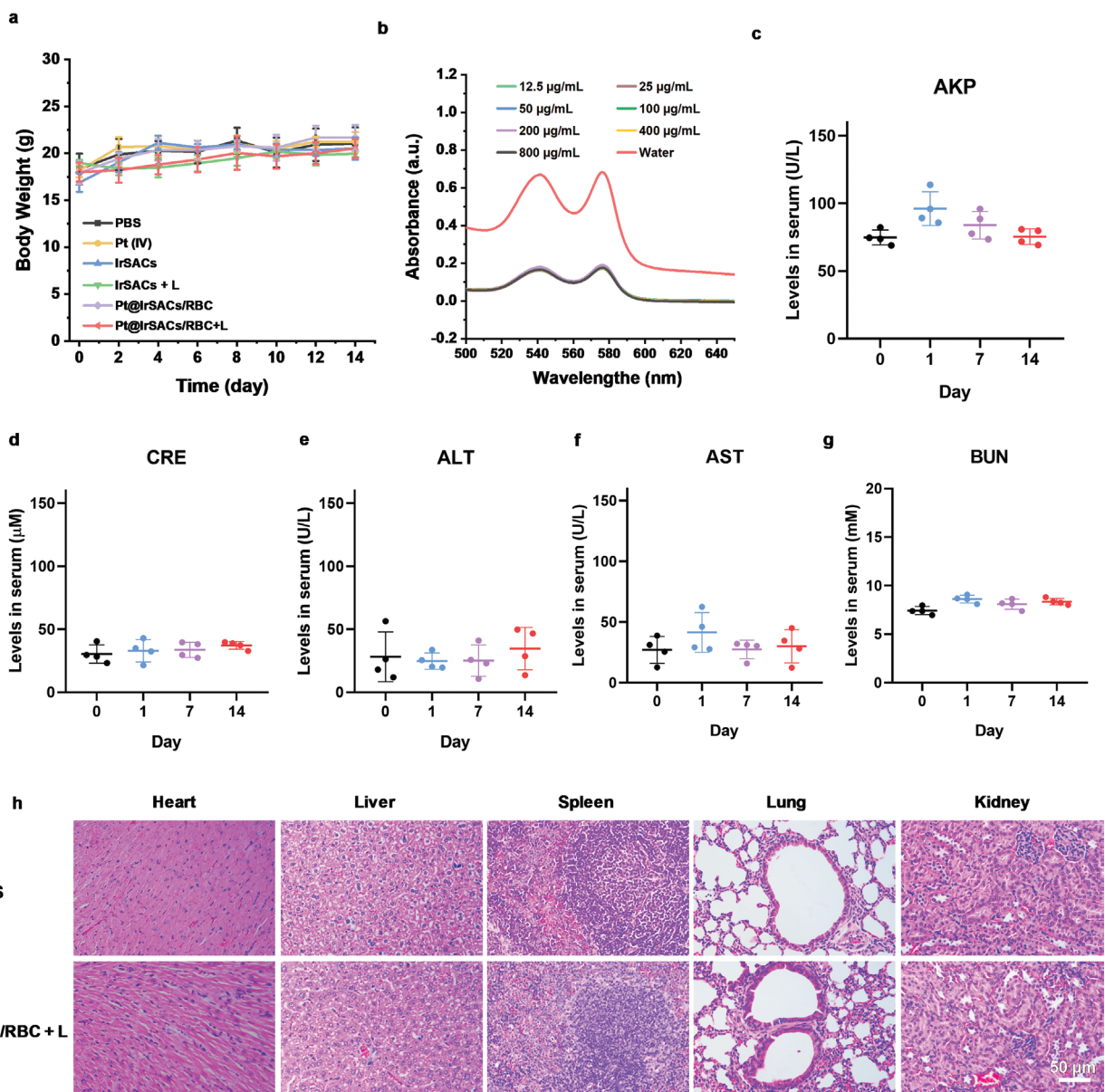


Figure 6. In vivo safety of Pt@IrSAC/RBC. a) Body weight of mice after treatment. b) Corresponding hemolysis test of Pt@IrSAC/RBC at different concentrations. c–g) Serum biochemistry parameters, including AKP (c), CRE (d), ALT (e), AST (f), and BUN (g) levels, were determined on the first, seventh, and 14th days after administration. h) Histological microscopic images stained with H&E.

included within the reference range values, which suggests that Pt@IrSAC/RBC caused no overt renal or hepatic toxicity in mice (Figure 6c–g). Furthermore, after sacrificing the mice, major organs were collected and analyzed by H&E staining (Figure S38, Supporting Information). No obvious tissue injury can be observed, suggesting the good biosafety of Pt@IrSAC/RBC.

3. Conclusion

We have developed an ultralow metal content IrSAC with fully exposed active sites. By coordinating with Pt(IV), the Pt@IrSACs/RBC represent remarkable catalytic activity to

amplify the potency of cellular ROS accumulation. The combination of catalytic and PTT therapy dramatically augmented tumor cell ferroptosis. Pt@IrSACs/RBC administered intravenously with 1064 nm irradiation post 24 h injection produced strong antitumor efficacy with negligible side effect. The tumors were completely ablated with a single treatment session and no tumor recurrence was observed. Our work presents a novel strategy to maximize the catalytic efficiency of SACs at an ultralow metal content and demonstrates their excellent therapeutic efficacy and biosafety in mouse triple-negative mammary carcinoma for the first time. As nanomedicine speeds ahead, efficient SACs with high biosafety may magnify a promising direction for the exploration of catalytic nanotherapy.

Supporting Information

Supporting Information is available from the Wiley Online Library or from the author.

Acknowledgements

J.C., L.L., and D.J. contributed equally to this work. This work was supported by the National Key R&D Program of China (2020YFA0710700, 2017YFA0505400), the National Natural Science Foundation of China (52021002, 21877103, 22177109, 32101121), users with Excellence Program of Hefei Science Center CAS (2020HSC-UE016), the Fundamental Research Funds for the Central Universities (WK3450000007), the National University of Singapore Start-up Grant (NUHSRO/2020/133/Startup/08), NUS School of Medicine Nanomedicine Translational Research Programme (NUHSRO/2021/034/TRP/09/Nanomedicine), and National Medical Research Council (NMRC) Centre Grant Programme (CG21APR1005). The authors gratefully appreciate Prof. Yue Yuan (USTC) for instrument support. All animal procedures were performed in accordance with the guidelines for Care and Use of Laboratory Animals of University of Science and Technology of China, and approved by the Animal Ethics Committee of University of Science and Technology of China (accreditation number: PXHG-LYZ2021041519). The TOC image was created with BioRender.com (2022).

Conflict of Interest

The authors declare no conflict of interest.

Data Availability Statement

The data that support the findings of this study are available from the corresponding author upon reasonable request.

Keywords

catalytic therapy, ferroptosis, nanocatalysts, single-atom catalysts, tumor therapy

Received: October 30, 2022

Revised: December 30, 2022

Published online: March 16, 2023

[1] a) X. Lu, S. Gao, H. Lin, J. Shi, *Small* **2021**, *17*, 2004467; b) S. Dong, Y. Dong, B. Liu, J. Liu, S. Liu, Z. Zhao, W. Li, B. Tian, R. Zhao, F. He, S. Gai, Y. Xie, P. Yang, Y. Zhao, *Adv. Mater.* **2022**, *34*, 2107054; c) B. Liu, S. Liang, Z. Wang, Q. Sun, F. He, S. Gai, P. Yang, Z. Cheng, J. Lin, *Adv. Mater.* **2021**, *33*, 2101223; d) W. Wang, Y. Zhu, X. Zhu, Y. Zhao, Z. Xue, C. Xiong, Z. Wang, Y. Qu, J. Cheng, M. Chen, M. Liu, F. Zhou, H. Zhang, Z. Jiang, Y. Hu, H. Zhou, H. Wang, Y. Li, Y. Liu, Y. Wu, *ACS Appl. Mater. Interfaces* **2021**, *13*, 45269; e) Y. Zhu, Y. Pan, Z. Guo, D. Jin, W. Wang, M. Liu, M. Zong, X. Zheng, Y. Wu, L. Wang, C. Tian, J. Cheng, Y. Liu, *Adv. Healthcare Mater.* **2022**, <https://doi.org/10.1002/adhm.202202198>.

[2] a) T. Qin, S. Ma, X. Miao, Y. Tang, D. Huangfu, J. Wang, J. Jiang, N. Xu, Y. Yin, S. Chen, X. Liu, Y. Yin, D. Peng, L. Gao, *Adv. Sci.* **2020**, *7*, 2000771; b) K. Fan, J. Xi, L. Fan, P. Wang, C. Zhu, Y. Tang, X. Xu,

M. Liang, B. Jiang, X. Yan, L. Gao, *Nat. Commun.* **2018**, *9*, 1440; c) Y. Zhu, D. Jin, M. Liu, Y. Dai, L. Li, X. Zheng, L. Wang, A. Shen, J. Yu, S. Wu, Y. Wu, K. Zhong, J. Cheng, Y. Liu, *Small* **2022**, *18*, e2200116; d) Y. Pan, Y. Zhu, C. Xu, C. Pan, Y. Shi, J. Zou, Y. Li, X. Hu, B. Zhou, C. Zhao, Q. Gao, J. Zhang, A. Wu, X. Chen, J. Li, *ACS Nano* **2022**, *16*, 19038.

- [3] a) Y. Zhou, X. Tao, G. Chen, R. Lu, D. Wang, M. X. Chen, E. Jin, J. Yang, H. W. Liang, Y. Zhao, X. Feng, A. Narita, K. Mullen, *Nat. Commun.* **2020**, *11*, 5892; b) D. Jin, M. Liu, M. Zhang, W. Yu, J. Yu, A. Shen, J. Cheng, Y. Liu, *Adv. Drug Delivery Rev.* **2023**, *192*, 114648.
[4] Z. Chen, L. Chen, C. Yang, Q. Jiang, J. Mater. Chem. A **2019**, *7*, 3492.
[5] Y. Peng, B. Lu, S. Chen, *Adv. Mater.* **2018**, *30*, 1801995.
[6] S. Li, N. Wang, Y. Yue, G. Wang, Z. Zu, Y. Zhang, *Chem. Sci.* **2015**, *6*, 2495.
[7] a) A. E. Nel, L. Madler, D. Velegol, T. Xia, E. M. Hoek, P. Somasundaran, F. Klaessig, V. Castranova, M. Thompson, *Nat. Mater.* **2009**, *8*, 543; b) Y. Wang, A. Santos, A. Evdokiou, D. Losic, *J. Mater. Chem. B* **2015**, *3*, 7153.
[8] a) Z. Song, L. Zhang, K. Doyle-Davis, X. Fu, J. L. Luo, X. Sun, *Adv. Energy Mater.* **2020**, *10*, 2001561; b) L. Qin, J. Gan, D. Niu, Y. Cao, X. Duan, X. Qin, H. Zhang, Z. Jiang, Y. Jiang, S. Dai, Y. Li, J. Shi, *Nat. Commun.* **2022**, *13*, 91; c) X. Luo, Z. Luo, X. Wei, L. Jiao, Q. Fang, H. Wang, J. Wang, W. Gu, L. Hu, C. Zhu, *Anal. Chem.* **2022**, *94*, 1390.
[9] X. F. Yang, A. Wang, B. Qiao, J. Li, J. Liu, T. Zhang, *Acc. Chem. Res.* **2013**, *46*, 1740.
[10] Q. Wang, Z. Zhang, C. Cai, M. Wang, Z. L. Zhao, M. Li, X. Huang, S. Han, H. Zhou, Z. Feng, L. Li, J. Li, H. Xu, J. S. Francisco, M. Gu, *J. Am. Chem. Soc.* **2021**, *143*, 13605.
[11] a) C. Wang, F. Lan, Z. He, X. Xie, Y. Zhao, H. Hou, L. Guo, V. Murugadoss, H. Liu, Q. Shao, Q. Gao, T. Ding, R. Wei, Z. Guo, *ChemSusChem* **2019**, *12*, 1576; b) X. Shao, X. Yang, J. Xu, S. Liu, S. Miao, X. Liu, X. Su, H. Duan, Y. Huang, T. Zhang, *Chem* **2019**, *5*, 693.
[12] a) D. Y. Zhang, Y. Zheng, H. Zhang, J. H. Sun, C. P. Tan, L. He, W. Zhang, L. N. Ji, Z. W. Mao, *Adv. Sci.* **2018**, *5*, 1800581; b) K. N. Wang, L. Y. Liu, G. Qi, X. J. Chao, W. Ma, Z. Yu, Q. Pan, Z. W. Mao, B. Liu, *Adv. Sci.* **2021**, *8*, 2004379; c) C. Wu, K. J. Wu, J. B. Liu, W. Wang, C. H. Leung, D. L. Ma, *Chem. Sci.* **2020**, *11*, 11404; d) Y. Yang, L. Guo, Z. Tian, Y. Gong, H. Zheng, S. Zhang, Z. Xu, X. Ge, Z. Liu, *Inorg. Chem.* **2018**, *57*, 11087.
[13] Y. Liu, B. Wang, J. Zhu, X. Xu, B. Zhou, Y. Yang, *Adv. Mater.* **2022**, *35*, 2208512.
[14] a) M. Xiao, J. Zhu, G. Li, N. Li, S. Li, Z. P. Cano, L. Ma, P. Cui, P. Xu, G. Jiang, H. Jin, S. Wang, T. Wu, J. Lu, A. Yu, D. Su, Z. Chen, *Angew. Chem., Int. Ed.* **2019**, *58*, 9640; b) J. Feng, F. Lv, W. Zhang, P. Li, K. Wang, C. Yang, B. Wang, Y. Yang, J. Zhou, F. Lin, G. C. Wang, S. Guo, *Adv. Mater.* **2017**, *29*, 1703798; c) Y. T. Kim, P. P. Lopes, S. A. Park, A. Y. Lee, J. Lim, H. Lee, S. Back, Y. Jung, N. Danilovic, V. Stamenkovic, J. Erlebacher, J. Snyder, N. M. Markovic, *Nat. Commun.* **2017**, *8*, 1449.
[15] a) T. J. Monks, R. P. Hanzlik, G. M. Cohen, D. Ross, D. G. Graham, *Toxicol. Appl. Pharmacol.* **1992**, *112*, 279. b) E. M. Malik, C. E. Muller, *Med. Res. Rev.* **2016**, *36*, 705.
[16] X. C. Huang, Y. Y. Lin, J. P. Zhang, X. M. Chen, *Angew. Chem., Int. Ed.* **2006**, *45*, 1557.
[17] a) E. Proietti, F. Jaouen, M. Lefèvre, N. Larouche, J. Tian, J. Herranz, J.-P. Dodelet, *Nat. Commun.* **2011**, *2*, 416; b) Y. Xiong, J. Dong, Z.-Q. Huang, P. Xin, W. Chen, Y. Wang, Z. Li, Z. Jin, W. Xing, Z. Zhuang, *Nat. Nanotechnol.* **2020**, *15*, 390.
[18] M. Xiao, J. Zhu, G. Li, N. Li, S. Li, Z. P. Cano, L. Ma, P. Cui, P. Xu, G. Jiang, *Angew. Chem., Int. Ed.* **2019**, *58*, 9640.
[19] S. Bawazeer, D. F. A. El-Telbany, M. M. Al-Sawahli, G. Zayed, A. A. A. Keed, A. E. Abdelaziz, D. H. Abdel-Naby, *Drug Delivery* **2020**, *27*, 1218.

- [20] P. Zhang, D. Sun, A. Cho, S. Weon, S. Lee, J. Lee, J. W. Han, D. P. Kim, W. Choi, *Nat. Commun.* **2019**, *10*, 940.
- [21] Z. Zhou, H. Liang, R. Yang, Y. Yang, J. Dong, Y. Di, M. Sun, *Angew. Chem., Int. Ed.* **2022**, *61*, 202202843.
- [22] M. Huo, L. Wang, Y. Wang, Y. Chen, J. Shi, *ACS Nano* **2019**, *13*, 2643.
- [23] C. Ruan, C. Liu, H. Hu, X. L. Guo, B. P. Jiang, H. Liang, X. C. Shen, *Chem. Sci.* **2019**, *10*, 4699.
- [24] Y. C. Geng, X. X. Wang, Y. Ma, Y. Hu, R. L. Zhang, *World J. Gastroenterol.* **1998**, *4*, 326.
- [25] M. Zan, J. Li, M. Huang, S. Lin, D. Luo, S. Luo, Z. Ge, *Biomater. Sci.* **2015**, *3*, 1147.
- [26] D. K. Roper, W. Ahn, M. Hoepfner, *J. Phys. Chem. C* **2007**, *111*, 3636.
- [27] H. S. Jung, J.-H. Lee, K. Kim, S. Koo, P. Verwilst, J. L. Sessler, C. Kang, J. S. Kim, *J. Am. Chem. Soc.* **2017**, *139*, 9972.
- [28] a) Z. Wang, Y. Zhang, E. Ju, Z. Liu, F. Cao, Z. Chen, J. Ren, X. Qu, *Nat. Commun.* **2018**, *9*, 3334; b) J. Li, L. Pan, W. G. Pembroke, J. E. Rexach, M. I. Godoy, M. C. Condron, A. G. Alvarado, M. Harteni, Y. W. Chen, L. Stiles, A. Y. Chen, I. B. Wanner, X. Yang, S. A. Goldman, D. H. Geschwind, H. I. Kornblum, Y. Zhang, *Nat. Commun.* **2021**, *12*, 3958.
- [29] Y. Zhu, W. Wang, J. Cheng, Y. Qu, Y. Dai, M. Liu, J. Yu, C. Wang, H. Wang, S. Wang, C. Zhao, Y. Wu, Y. Liu, *Angew. Chem., Int. Ed.* **2021**, *60*, 9480.
- [30] Y. Dai, Y. Zhu, J. Cheng, J. Shen, H. Huang, M. Liu, Z. Chen, Y. Liu, *Chem. Commun.* **2020**, *56*, 14051.
- [31] a) T. Kirkegaard, A. G. Roth, N. H. Petersen, A. K. Mahalka, O. D. Olsen, I. Moilanen, A. Zylizc, J. Knudsen, K. Sandhoff, C. Arenz, P. K. Kinnunen, J. Nylandsted, M. Jaattela, *Nature* **2010**, *463*, 549; b) L. Fernandez-Mosquera, K. F. Yambire, R. Couto, L. Pereyra, K. Pabis, A. H. Ponsford, C. V. Diogo, M. Stagi, I. Milosevic, N. Raimundo, *Autophagy* **2019**, *15*, 1572.
- [32] a) J. Cheng, Y. Zhu, X. Xing, J. Xiao, H. Chen, H. Zhang, D. Wang, Y. Zhang, G. Zhang, Z. Wu, Y. Liu, *Theranostics* **2021**, *11*, 5418; b) M. Gao, P. Monian, Q. Pan, W. Zhang, J. Xiang, X. Jiang, *Cell Res.* **2016**, *26*, 1021.
- [33] L. Zou, J. Lu, J. Wang, X. Ren, L. Zhang, Y. Gao, M. E. Rottenberg, A. Holmgren, *EMBO Mol. Med.* **2017**, *9*, 1165.
- [34] Q. Weng, H. Sun, C. Fang, F. Xia, H. Liao, J. Lee, J. Wang, A. Xie, J. Ren, X. Guo, F. Li, B. Yang, D. Ling, *Nat. Commun.* **2021**, *12*, 1436.
- [35] A. Tarangelo, L. Magtanong, K. T. Biegling-Rolett, Y. Li, J. Ye, L. D. Attardi, S. J. Dixon, *Cell Rep.* **2018**, *22*, 569.
- [36] W. S. Yang, R. SriRamaratnam, M. E. Welsch, K. Shimada, R. Skouta, V. S. Viswanathan, J. H. Cheah, P. A. Clemons, A. F. Shamji, C. B. Clish, L. M. Brown, A. W. Girotti, V. W. Cornish, S. L. Schreiber, B. R. Stockwell, *Cell* **2014**, *156*, 317.
- [37] M. Chang, Z. Hou, M. Wang, C. Yang, R. Wang, F. Li, D. Liu, T. Peng, C. Li, J. Lin, *Angew. Chem., Int. Ed.* **2021**, *60*, 12971.
- [38] X. Zhang, Y. Liu, S. Gopalakrishnan, L. Castellanos-Garcia, G. Li, M. Malassine, I. Uddin, R. Huang, D. C. Luther, R. W. Vachet, V. M. Rotello, *ACS Nano* **2020**, *14*, 4767.
- [39] Z. Jiang, Y. Chu, C. Zhan, *Expert Opin. Drug Delivery* **2022**, *19*, 833.
- [40] W. Gao, L. Zhang, *AIChE J.* **2015**, *61*, 738.
- [41] W. Gao, C. M. Hu, R. H. Fang, B. T. Luk, J. Su, L. Zhang, *Adv. Mater.* **2013**, *25*, 3549.
- [42] a) F. Yuan, M. Dellian, D. Fukumura, M. Leunig, D. A. Berk, V. P. Torchilin, R. K. Jain, *Cancer Res.* **1995**, *55*, 3752; b) J. Fang, H. Nakamura, H. Maeda, *Adv. Drug Delivery Rev.* **2011**, *63*, 136.
- [43] J. Piao, L. Wang, F. Gao, Y. You, Y. Xiong, L. Yang, *ACS Nano* **2014**, *8*, 10414.
- [44] a) L. Yan, F. Zhao, J. Wang, Y. Zu, Z. Gu, Y. Zhao, *Adv. Mater.* **2019**, *31*, 1805391; b) Z. Li, J. Zou, X. Chen, *Adv. Mater.* **2022**, <https://doi.org/10.1002/adma.202209529>.